

# A Sensorized Multi-Joint Manikin for Measuring Force and Torque Profiles of Back-Support Exoskeletons

Haibing Tian<sup>a</sup>, Tom Turcksin<sup>a,b</sup>, Huaijin Chen<sup>c</sup>, Joost Geeroms<sup>a,b</sup>, Tom Verstraten<sup>a,b</sup>, Bram Vanderborght<sup>a,b,c</sup>

<sup>a</sup>Brubotics, Pleinlaan 2, Brussels, 1050, Belgium

<sup>b</sup>Flanders Make, Oude Diestersebaan 133, Lommel, 3920, Belgium

<sup>c</sup>Imec, Kapeldreef 75, Leuven, 3001, Belgium

---

## Abstract

Occupational back-support exoskeletons are increasingly being adopted to mitigate physical strain on workers. However, mechanical characterization of these devices remains insufficient. This study introduces a sensorized multi-joint manikin designed for consistent assessment of exoskeleton–body mechanical interactions. The manikin incorporates simulated L5–S1 and hip joints and integrates 28 load cells distributed across the torso, buttocks, and thighs, enabling localized force measurements summed into segmental forces. These segmental forces were further used to compute the assistive hip torque ( $T_{hip}$ ) and the overall resultant force ( $F_r$ ) during multi-joint motion. To validate the manikin, a lower-body-driven trunk flexion–extension task was performed for three repeated cycles using the Laevo FLEX exoskeleton. Support vector regression models were trained on experimental data from three trials and subsequently used to predict segmental forces,  $F_r$ , and  $T_{hip}$  along a representative flexion–extension trajectory. The predicted segmental force profiles exhibited changes near specific joint transitions, suggesting sensitivity to inter-joint coordination. Predicted  $F_r$  remained within 12 N under quasi-static movements, confirming approximate force equilibrium at the system level and indirectly supporting the reliability of segmental force measurements. Additionally, predicted  $T_{hip}$  showed pronounced hysteresis without saturation, likely reflecting combined joint coordination effects and interface displacement. These findings underscore the influence of joint coordination on mechanical interactions and emphasize the importance of considering inter-joint dynamics in both exoskeleton design and biomechanical performance analysis. Overall, the proposed sensorized manikin offers a generalizable framework for evaluating mechanical performance across exoskeletons and may provide experimental inputs for future biomechanical modeling.

**Keywords:** back-support exoskeleton, sensorized manikin, force measurement, joint coordination

---

## 1. Introduction

Low back pain (LBP) remains one of the most prevalent work-related musculoskeletal disorders, affecting over one-fourth of workers globally and imposing substantial economic burdens (Luckhaupt et al., 2019). Beyond absenteeism and reduced productivity, LBP imposes considerable economic burdens (Olafsson et al., 2018; Wenig et al., 2009), underscoring the need for ergonomic interventions that support spinal health without limiting worker mobility (Hilmi et al., 2024).

Occupational back-support exoskeletons have emerged as promising ergonomic solutions to mitigate LBP in industrial settings (Theurel and Desbrosses, 2019; van Sluijs et al., 2023; Brouwer et al., 2024). Their biomechanical performance—typically evaluated via muscle activity measurements—has been widely studied (Wei et al., 2020; Koopman et al., 2020b; Weston et al., 2018). However, their physical interaction with the human body remains underexplored. A recent review identified 54 studies on physical human–exoskeleton interaction (pHEI), but only three focused on back-support devices (Massardi et al., 2022). Among the key parameters in pHEI, interface forces and torques are essential not only for evaluating device comfort and safety, but also as external inputs in musculoskeletal simulations aimed at analyzing exoskeleton-induced biomechanical responses across diverse tasks (Madinei et al., 2022). Despite their importance, these data remain scarce due to limited disclosure from manufacturers, hindering comparative analysis and model fidelity.

Several efforts have attempted to directly measure interface forces applied by back-support exoskeletons to the human body, using force transducers on the chest (Koopman et al., 2019, 2020a) and force-sensitive resistors on the thigh (Choi et al., 2018). However, these approaches face challenges in achieving secure attachment on anatomically curved body surfaces. To improve contact fidelity, Wang et al. (2021) developed a soft pneumatic force sensor to measure normal forces between the human thigh and the exoskeleton. Despite this advancement, inter-individual variability in limb geometry and soft tissue compliance compromises sensor conformity and measurement accuracy. To complement human-subject studies and improve measurement repeatability, manikin-based platforms have been proposed as alternatives for quantifying physical interactions in wearable systems under controlled conditions (Dežman et al., 2023). For instance, Akiyama et al. (2012) developed a leg dummy equipped with force sensors to investigate how joint misalignment affects interface forces. Dežman et al. (2023) further built a leg replica with multi-axis force sensors to quantify physical interactions in lower-limb exoskeletons. While effective, these designs are specific to lower-limb applications and do not address trunk-level interactions. Madinei et al. (2022) proposed a hip-joint manikin to quantify assistive torque profiles in back-support exoskeletons, but it lacked force sensing. Moreover, by excluding lumbar motion, its single-joint configuration overlooks the potentially coupled behavior between the lumbar spine and hip during trunk flexion and extension, limiting its capacity to assess coordination effects that may influence mechanical loading dynamics and impact interaction fidelity in back-support exoskeletons.

To address these gaps, we present a sensorized multi-joint manikin capable of measuring mechanical interactions between back-support exoskeletons and the body during coordinated, bending-like motion. The manikin incorporates L5–S1 and hip joints and features 28 load cells distributed across the torso, buttocks, and thighs. This design enables repeatable, subject-independent experiments to quantify interaction forces and torques. The manikin also supports scalable evaluation across different exoskeletons and provides actionable mechanical insights to inform the design of back-support systems.

## 2. Methods

### 2.1. Manikin design and sensors

A sensorized manikin (see Figure 1) was developed to quantify manikin–exoskeleton mechanical interactions during simulated trunk flexion and extension. The manikin features a two-degree-of-freedom (DoF) articulated structure that represents motions of the L5–S1 and hip joints. Three subassemblies—torso, buttocks, and thighs—are connected via revolute joints and mounted to a fixed base. Joint ranges of motion and joint spacing were approximated based on anthropometric data, with implemented values listed in Supplementary Tables S1 and S2. Deviations from reported human measurements were accepted due to inter-individual variability and structural constraints of the experimental setup. The manikin was configured such that flexion–extension motion at the L5–S1 and hip joints was induced by manually pulling the distal structure, while the torso subassembly remained stationary.

To measure interaction forces, 28 WWZMDiB load cells were embedded across the torso, buttocks, and thighs. These load cells capture normal and tangential forces at the manikin–exoskeleton interfaces and are grouped into six segmental forces based on Supplementary Eqs. (1)–(6).

### 2.2. Calibration experiments

To ensure reliable force measurements, a two-stage calibration procedure was implemented. First, each load cell was individually calibrated using known weights to establish a linear voltage–force relationship. Second, subassembly-level calibration was performed to evaluate measurement accuracy (MA) and cross-axis interference (CI) by applying known loads and analyzing the combined response of load cells within each subassembly. For the thigh subassembly, the left and right sides were calibrated separately. The thigh subassembly calibration (Figure 2) included 9  $\mathbf{F}_N$  and 4  $\mathbf{F}_T$  calibration points. In total, 46 points were tested across all three subassemblies: 26 on the bilateral thighs (13 per side), and 10 each on the buttocks and torso. The number of calibration points varied due to geometric constraints.

### 2.3. Experimental procedures

The manikin’s legs were manually moved to induce flexion–extension at the hip and L5–S1 joints, with load cell signals and marker trajectories simultaneously recorded. The experimental protocol comprised two phases:

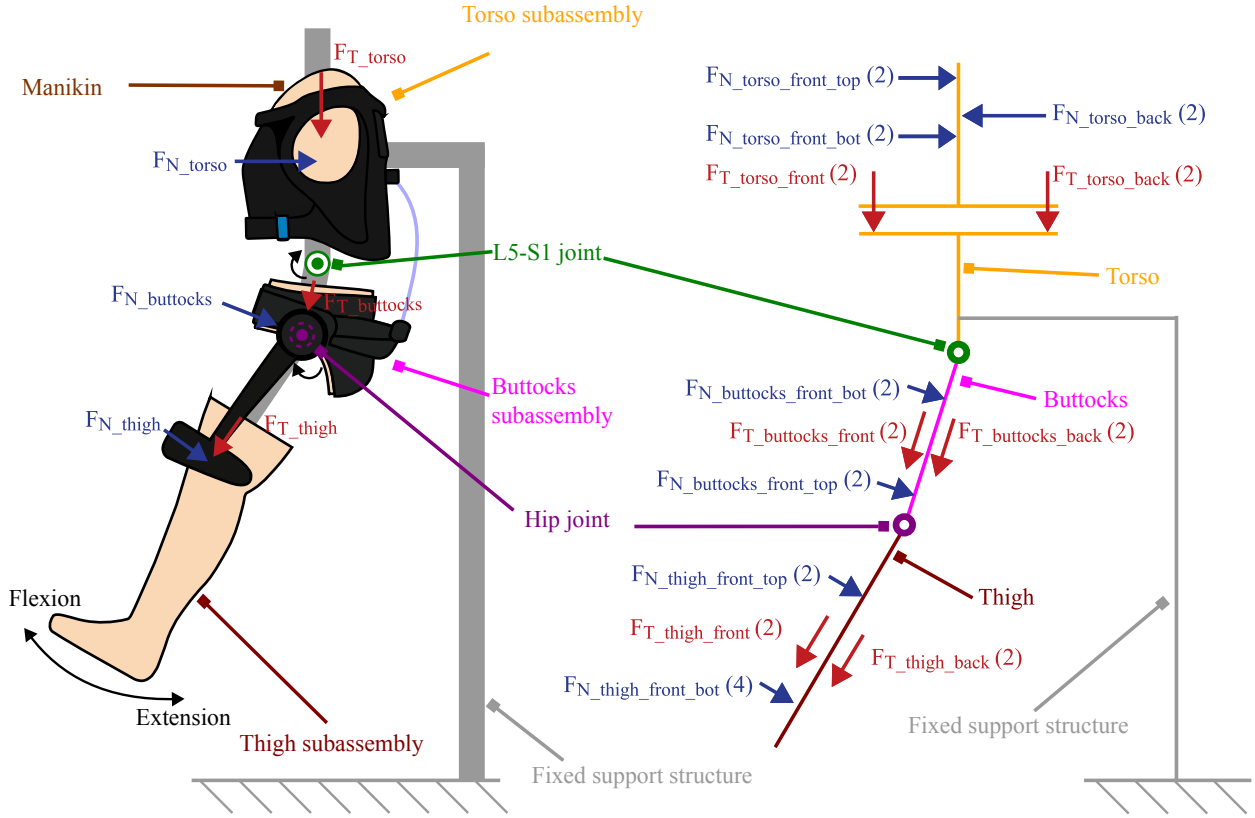


Figure 1: Schematic side view of the manikin, comprising a structural diagram (left) and force measurement schematic (right). The left panel shows three subassemblies—the torso (orange), buttocks (fuchsia), and thigh (maroon)—mounted on a fixed support structure (gray) and interconnected via revolute joints: the L5-S1 joint (green) and hip joints (purple). Six exoskeleton-induced segmental resultant forces—normal and tangential components for each subassembly—are calculated via vector summation of load cell readings at each segment. The right panel specifies load cell positions, force directions, and the number of sensors used per force component (indicated in parentheses), arranged symmetrically about the sagittal plane. Arrows indicate positive directions. Boldface (e.g.,  $\mathbf{F}_T$ ) denotes vectors; plain text ( $F_T$ ) indicates scalar magnitudes. The force nomenclature follows a tripartite format: [type][subassembly][location]. Here, the type includes  $\mathbf{F}_T$  (tangential force) and  $\mathbf{F}_N$  (normal force); the subassembly includes torso, buttocks, or thigh; and load cell location (e.g., front\_top). For example,  $\mathbf{F}_{N,torso,front\_top}$  refers to the normal force vector at the torso's anterior-superior region, with its direction aligned with the annotated arrow.

(1) Baseline (no exoskeleton): 20 flexion–extension cycles were performed to characterize gravitational force effects.

(2) Assisted trials: As a validation case, the Laevo FLEX exoskeleton—with medium-stiffness gas springs—was used to demonstrate the platform's measurement capabilities. The exoskeleton was mounted on the manikin with bilateral rotational centers aligned to the hip joints (Figure 3). Following this, the same motion was performed for three cycles at low speed to approximate quasi-static conditions, minimizing inertial effects.

#### 2.4. Data acquisition and processing

In this study, analog voltage signals from all load cells and trajectories of retroreflective markers were sampled at 100 Hz using a Vicon motion capture system (Vicon, UK) equipped with the Lock+ analog acquisition interface.

During load-cell calibration, raw voltage signals were low-pass filtered (4<sup>th</sup>-order zero-lag Butterworth, 5 Hz), offset-corrected, and regressed against known forces in MATLAB to compute force-to-voltage coefficients. These coefficients were used to convert raw outputs into segmental forces during subassembly-level calibration. Calibration quality was quantified using MA and CI, defined in Eqs. (7) and (8). Ideally, MA approaches 100% and CI approaches 0%.

Segmental forces during assisted trials were calculated by subtracting baseline forces from total measured forces, while joint angles (L5-S1 and hip, relative to the torso), joint center positions, and exoskeleton leg pad trajectories

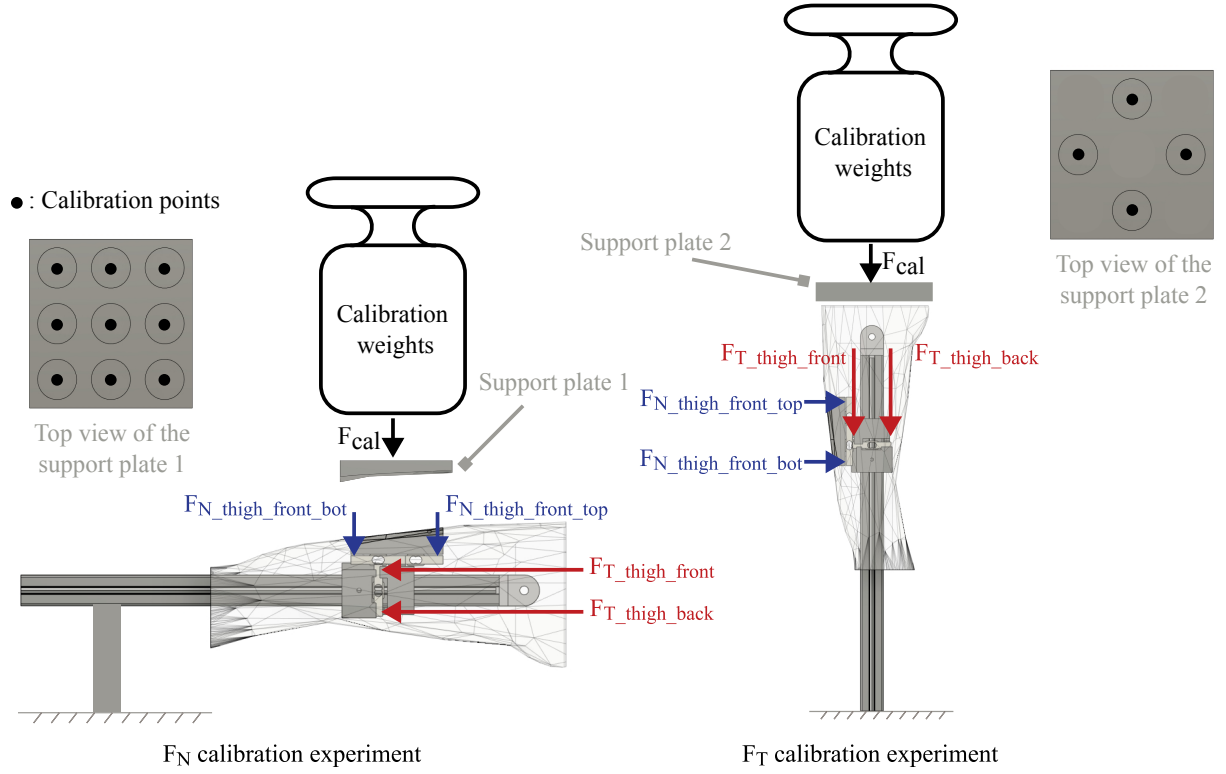


Figure 2: Thigh subassembly calibration (one side). Left and right panels illustrate the  $\mathbf{F}_N$  and  $\mathbf{F}_T$  calibration arrangements, respectively. Known forces ( $\mathbf{F}_{cal}$ ) were applied vertically using support plates that defined horizontal reference planes. Black dots on the plate top views indicate  $\mathbf{F}_{cal}$  application points—9 for  $\mathbf{F}_N$  and 4 for  $\mathbf{F}_T$ .

were concurrently derived from marker-based kinematic data. System-level resultant force ( $\mathbf{F}_r$ , Eq. 9) and assistive hip torque ( $\mathbf{T}_{hip}$ , Eq. 10) were computed to verify equilibrium and quantify exoskeleton assistance, respectively. These procedures yielded eight mechanical variables: six segmental forces,  $\mathbf{F}_r$ , and  $\mathbf{T}_{hip}$ , all of which were interpolated and resampled over joint angle grids to enable consistent, angle-based comparisons across trials. Inter-trial torque consistency was assessed using the intraclass correlation coefficient (ICC, Eq. (11)) and average normalized RMSE ( $Av_{gNRMSSE}$ , Eq. (12)), within stable and common angular ranges.

Variation in hip angle trajectories across trials prevented direct representation of system behavior using a single trial. Therefore, support vector regression (SVR) models were trained using hip angle as input and eight mechanical variables as outputs, enabling continuous, angle-based estimation of system responses across trials. Model predictive accuracy was evaluated across three trials using the coefficient of determination ( $R^2$ ). These trained models allowed the prediction of mechanical outputs under a representative hip angle trajectory defined by the average peak hip flexion angle across trials. The SVR-predicted torque–angle profile was then used to compute energy dissipation and hysteresis ratio.

### 3. Results

#### 3.1. MA and CI

Table S3 summarizes the calibration results from the subassembly-level calibration. All 46 calibration trials yielded MA values  $\geq 91\%$  and CI values  $\leq 5.5\%$ . Most trials achieved over 95% MA and less than 4% CI, demonstrating high measurement accuracy and negligible cross-axis interference.

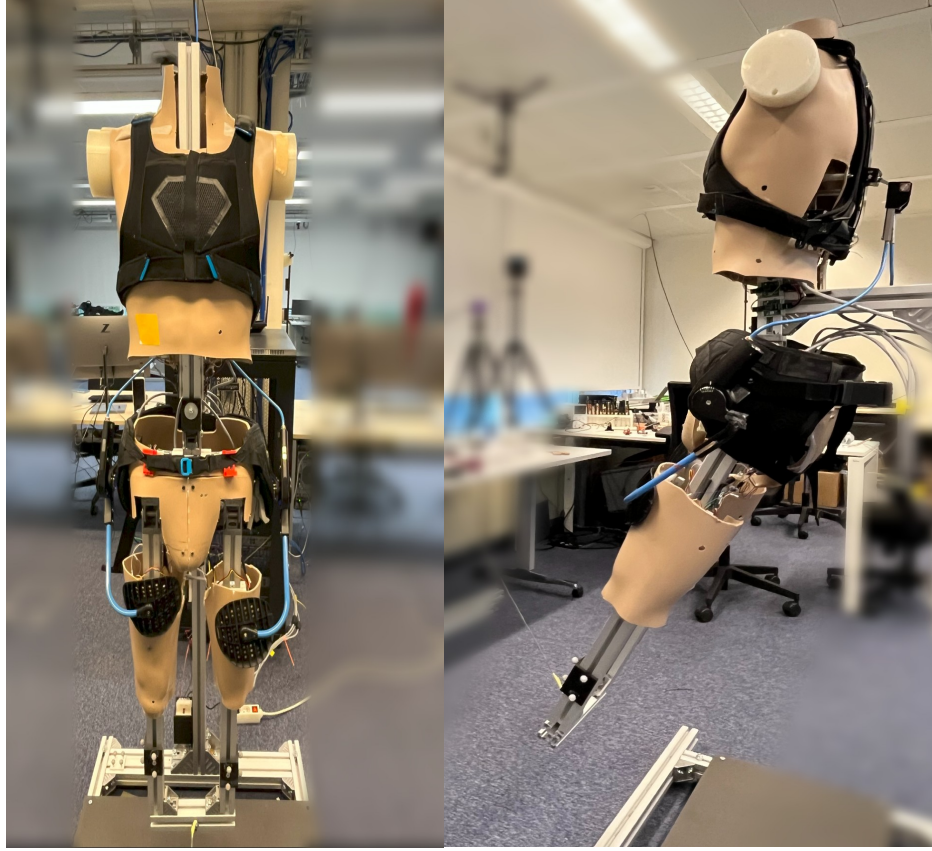


Figure 3: Frontal and lateral views of the manikin with the Laevo FLEX exoskeleton mounted.

### 3.2. Joint angles

Figure 4 presents the hip and L5–S1 joint angles during the second flexion–extension cycle with the exoskeleton. This cycle was chosen as an illustrative example for defining motion segmentation during joint coordination. The cycle was divided into five distinct stages based on six moments, identified from joint angle and velocity profiles.

(1) Early flexion (I–II): Flexion initiated at the L5–S1 joint approximately 1.5 seconds before the hip, followed by gradual motion at both joints.

(2) Late flexion (II–III): L5–S1 motion nearly plateaued, while hip flexion increased markedly, dominating the movement.

(3) Early extension (III–IV): Extension initiated at the hip approximately 2 seconds before the L5–S1 joint, with L5–S1 remaining largely stationary during this stage.

(4) Mid extension (IV–V): Both joints extended and shared contribution to the movement.

(5) Late extension (V–VI): The hip joint continued to extend, while the L5–S1 angle remained nearly unchanged.

Overall, L5–S1–hip coordination showed stage-specific patterns: flexion was initiated by the L5–S1, extension by the hip; dual-joint motion occurred in early flexion and mid extension, while late flexion, early extension, and late extension featured primarily single-joint motion. These patterns suggest asymmetry and stage-specific dynamics in L5–S1–hip coordination.

### 3.3. Forces

Figure 5 shows the SVR-predicted segmental force profiles based on a representative hip trajectory. Transition moments (I–VI) follow the same segmentation method as in Section 3.2, but are derived from the representative trajectory; Model prediction performance ( $R^2$ ) is reported in Table S4.

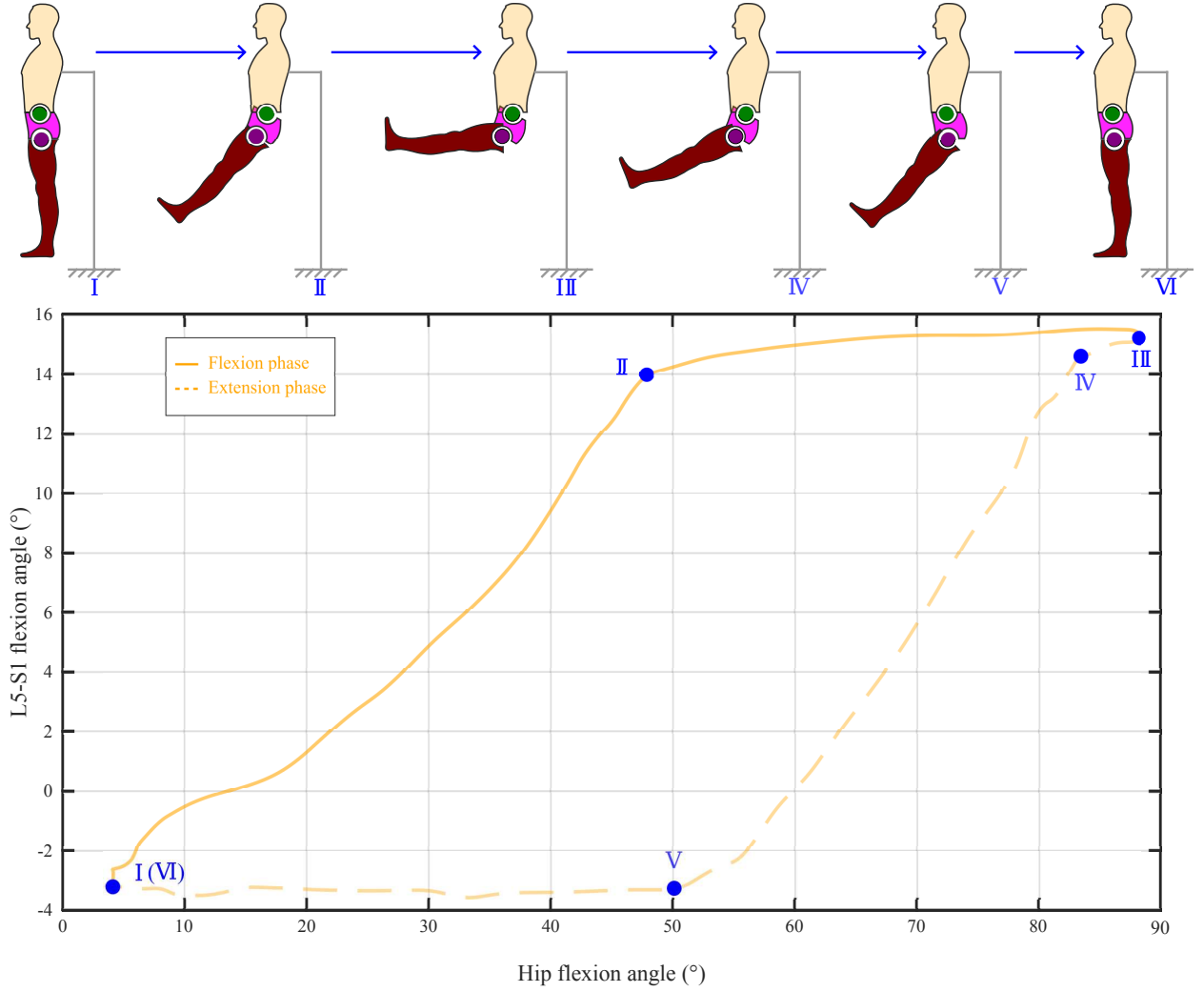


Figure 4: Measured hip and L5–S1 joint angles during the second flexion–extension cycle with the exoskeleton. The cycle is divided into five stages, based on six transition moments (I–VI). Above the angle–angle plot, schematic postures illustrate the manikin’s configuration at each key moment.

All segmental force profiles exhibited phase-dependent asymmetry, with tangential forces showing more pronounced divergence between flexion and extension trajectories than normal forces. Key transitions—such as moment III and moment IV—induced marked changes across nearly all force components. In contrast, moment V predominantly affected normal forces. Moment II caused noticeable responses in  $F_{N\_buttocks}$  and  $F_{T\_torso}$ , while other components remained largely unaffected.

Given the low angular acceleration observed across three trials ( $<0.5 \text{ rad/s}^2$ ), the system was treated as quasi-static. Accordingly,  $F_r$  was computed to verify mechanical equilibrium. As shown in Figure 6, the resultant force  $F_r$  predicted by the SVR model remained consistently low across the flexion–extension cycle, confirming near quasi-static conditions. The low residual may arise from minor inertial effects or calibration inaccuracies, but its magnitude—being well below the primary segmental forces—indirectly supports the reliability of the segmental force measurements.

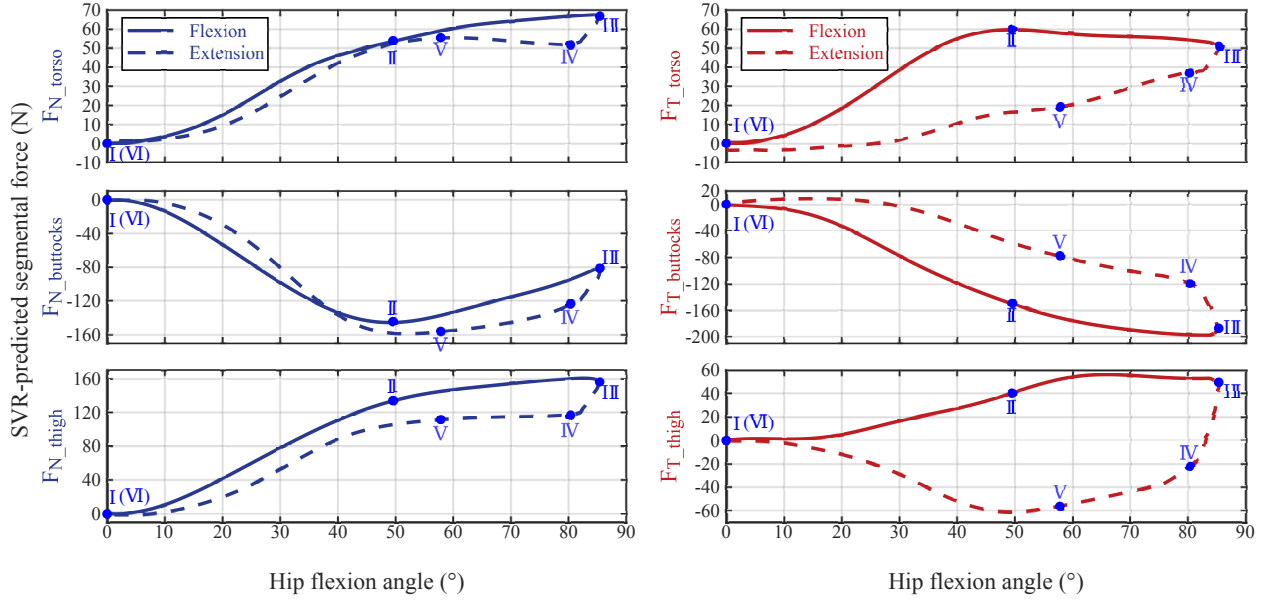


Figure 5: SVR-predicted segmental force–angle profiles. The left three subplots illustrate the normal forces, while the right three show the tangential forces, shown in dark blue and deep red, respectively. Each row corresponds to a different subassembly: the torso (top), the buttocks (middle), and the thigh (bottom).

### 3.4. Torques

Figure 7 shows the  $T_{hip}$ –angle profiles from three trials and the SVR-predicted curve. All profiles showed monotonic flexion without torque saturation and displayed pronounced hysteresis loops. Flexion ( $3.7^{\circ}$ – $82.2^{\circ}$ ) and extension ( $76^{\circ}$ – $7^{\circ}$ ) ranges shared across trials were analyzed to assess torque consistency. ICC and  $Av_{gNRMSSE}$  were computed within these shared ranges, exceeding 99.8% and remaining below 2%, respectively, indicating high inter-trial reproducibility.

## 4. Discussion

This study introduces a sensorized manikin for measuring mechanical interactions between back-support exoskeletons and the body during trunk-like flexion–extension. This design provides a generalizable tool for characterizing force and torque interactions in back-support wearable devices. The manikin captures normal and tangential segmental forces, as well as assistive torque, revealing how these interactions vary with L5–S1 and hip joint coordination. These measurements highlight significant coordination-dependent mechanical behaviors, underscoring the need to consider joint coordination in the analysis of exoskeleton mechanics.

This manikin adopts two key simplifications to facilitate platform design and enable interpretable evaluation of exoskeleton-induced mechanical interactions. First, the L5–S1 and hip joints were implemented as idealized hinge joints to permit sagittal-plane flexion and extension only, whereas anatomical joints exhibit multi-axial motion. This simplification reflects the dominant movement in trunk bending tasks and avoids introducing additional DoFs that would complicate mechanical design, sensor alignment, and force decomposition. Second, biological features such as ligaments, discs, and capsular compliance were omitted to maintain a rigid-body structure suitable for distributed force sensing. While these simplifications reduce anatomical fidelity, they do not impair the manikin’s utility as a generalizable tool for comparing mechanical interactions across different back-support exoskeletons under consistent experimental conditions.

The L5–S1 and hip joints exhibited sequential activation—L5–S1 leading flexion and the hip leading extension—along with a direction-dependent, non-overlapping angle–angle trajectory. While these coordination patterns were derived from a manikin-based L5–S1–hip configuration, they provide a simplified representation of lumbo–pelvic dynamics typically observed in human studies. For instance, Tsang et al. (2017) reported asymmetric lumbo–pelvic



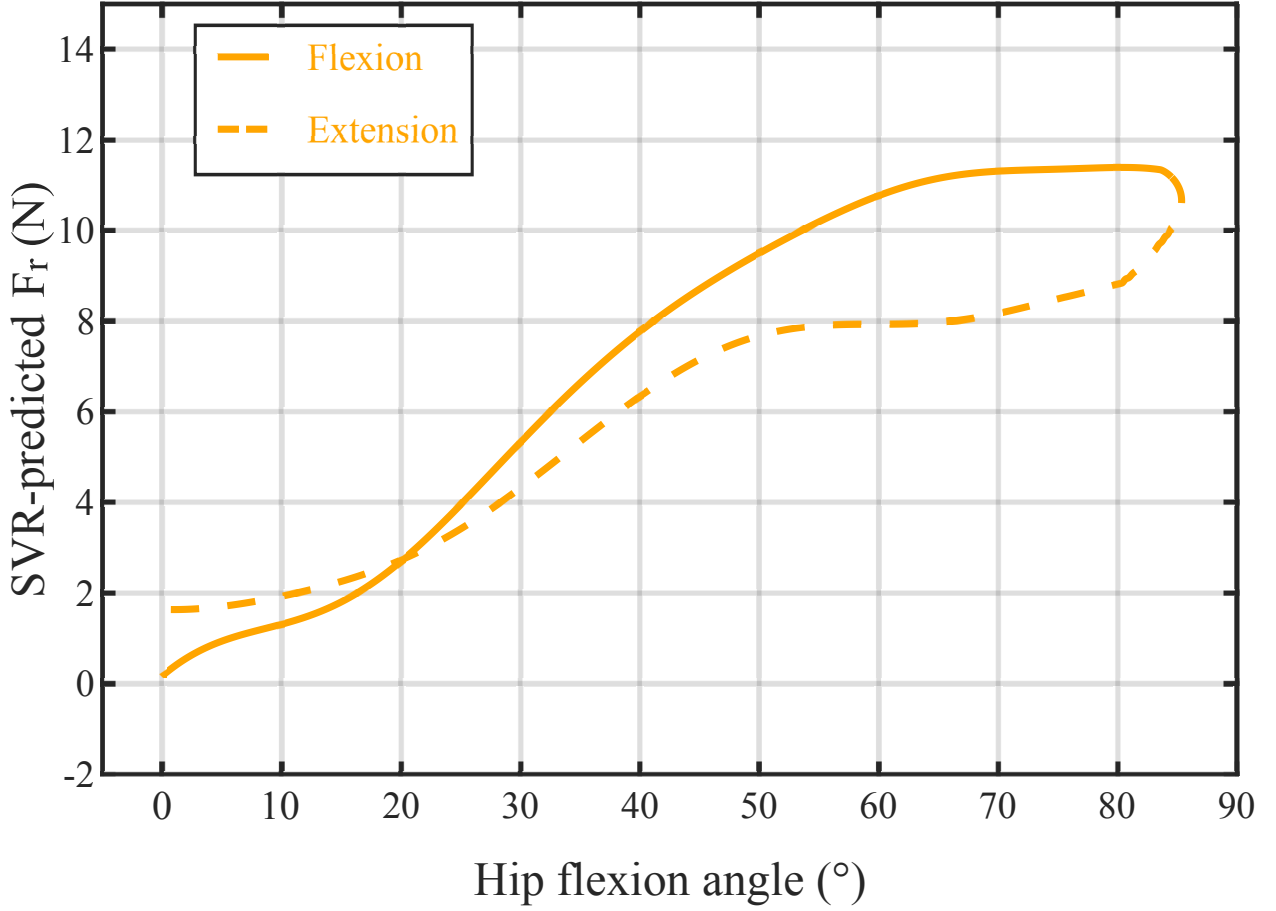


Figure 6: SVR-predicted  $F_r$ -angle profile. Throughout the cycle,  $F_r$  remained below 12 N, less than 6% of the maximum segmental force.

motion between flexion and extension at various bending speeds in asymptomatic individuals. Similarly, sequential motion between the lumbar spine and pelvis was reported by Thomas and Gibson (2007) and Pal et al. (2007), though with differences in timing. A systematic review by Vazirian et al. (2016) noted that the lumbar contribution predominates during the early stages of trunk flexion and the later stages of extension, with variations influenced by factors such as age and health status (e.g., presence of LBP). This coordination pattern has practical implications: many back-support exoskeletons rely on hip angle as the primary trigger for assistance. However, during early flexion—when motion is predominantly lumbar-driven—such systems may fail to activate appropriately, offering limited support as lumbar loading begins to increase. Taken together, our manikin-derived findings—particularly the observed sequential activation and direction-dependent trajectory between L5–S1 and the hip—underscore the importance of considering joint coordination patterns when designing back-support exoskeletons. While simplified, these patterns offer partial analogs to lumbo–pelvic dynamics reported in human studies, and may inform bio-inspired design strategies that enhance mechanical compatibility and motion congruence.

We quantified six segmental forces to characterize back-support exoskeleton interactions during flexion–extension. Only  $F_{N\_torso}$  shows directly comparable values in the literature, peaking at  $\sim 67$  N, aligning with human-subject measurements using Laevo V2.4 during static holding ( $\sim 75$  N) and Laevo V2.5 during repetitive lifting ( $\sim 55$  N) (Koopman et al., 2019; Eskandari et al., 2025). These differences likely reflect variations in device versions and task protocols, but the comparable magnitude supports the validity of our measurements. Although no literature comparisons exist for other forces, their quantification remains essential.  $F_{N\_thigh}$  and  $F_{N\_buttocks}$  provide mechanical stability through torque balancing and force equilibrium. However, excessive localized normal force can impair comfort by restricting blood flow or compressing soft tissues (Akiyama et al., 2015), influenced by the contact area,



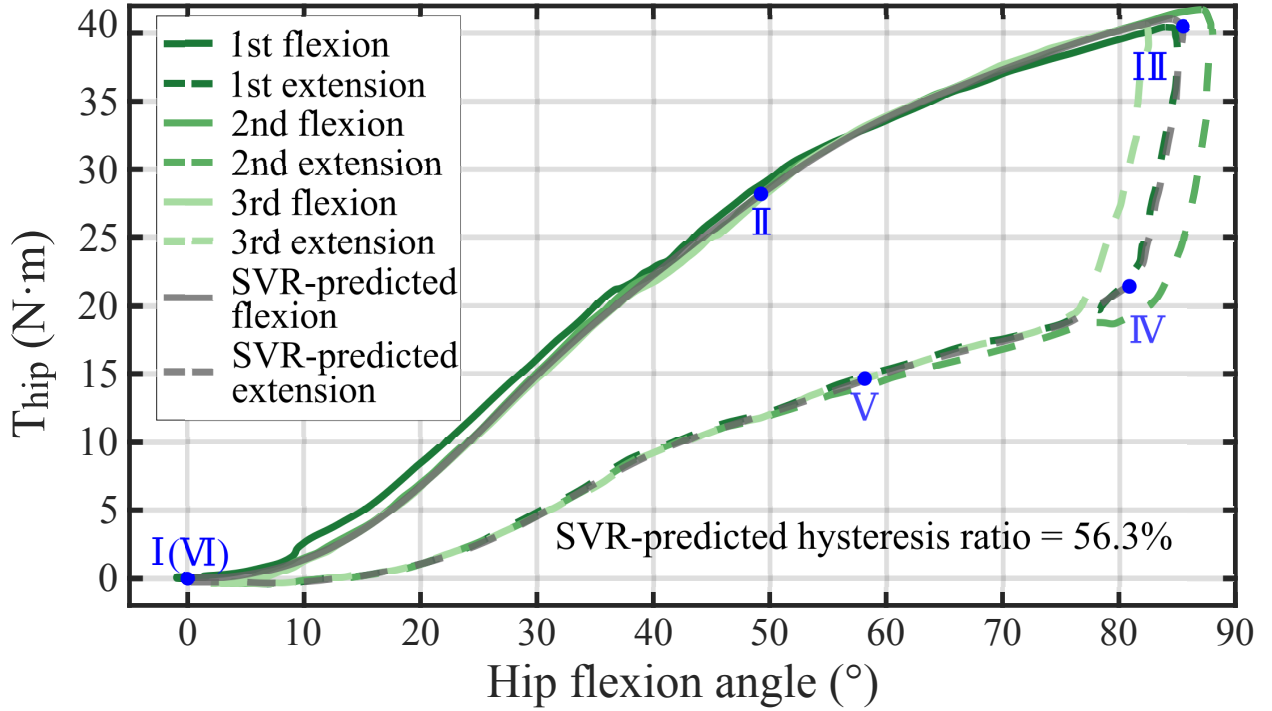


Figure 7: Hip torque-angle profiles from three trials and the SVR-predicted profile. Torque-angle profiles from the 1st, 2nd, and 3rd trials are shown in dark green, medium green, and light green, respectively. The SVR-predicted profile is plotted in medium gray. The SVR-predicted curve reached 41 N·m at maximum hip flexion and showed 56.3% hysteresis, corresponding to approximately 18 J of energy dissipation.

interface geometry, and material compliance (Bessler et al., 2021). Thus, accurately measuring these forces is vital for exoskeleton design strategies to optimize assistance and minimize discomfort. Tangential forces are also critical due to their association with skin injury risks (Armitage et al., 2021; Akiyama et al., 2015), yet often underreported because of measurement difficulties (Massardi et al., 2022). Early measurement via sensorized manikin platforms during development can guide refinements to reduce discomfort and injury potential during human use. In our study, tangential forces exhibited greater hysteresis than normal forces in force-angle profiles, likely due to relative interface motion (Langlois et al., 2020), joint coordination asymmetry, and the exoskeleton's gas spring (Van Harmelen et al., 2022). In contrast, normal forces are primarily governed by compression and are less susceptible to the aforementioned hysteresis-inducing factors, showing less pronounced hysteresis. Finally, our results demonstrate that joint coordination has a significant impact on interface forces. Thomas and Gibson (2007) observed that hip extension precedes lumbar motion by 63 ms in humans, whereas in our experiment, hip extension preceded L5-S1 extension by approximately 2 seconds. Had the L5-S1 motion followed more closely behind the hip, the force-angle profiles might have shifted earlier (see Fig. 4), aligning moment IV with moment III and potentially reducing the observed hysteresis. Furthermore, if the L5-S1 motion had progressed more smoothly throughout both flexion and extension, the  $F_{N\_buttocks}$  profile might have exhibited more monotonic behavior within each phase. These hypotheses could be validated in future work by regulating joint kinematics using motorized actuation. Together, these findings underscore the importance of quantifying segmental forces and considering joint coordination to facilitate accurate evaluation and informed exoskeleton design.

The assistive torque-angle profile exhibited a continued rise during flexion and a pronounced hysteresis loop (~56.3%), exceeding the saturation torque level (40 N·m) reported in a previous single-joint setup using the same exoskeleton (Van Harmelen et al., 2022). In that configuration, assistive torque plateaued beyond ~40° of hip flexion with a lower hysteresis ratio of 34%. Notably, in our experiment, both  $F_{N\_thigh}$  and  $F_{T\_thigh}$  exhibited minimal variation beyond 65° hip flexion, suggesting that the continued torque rise is not due to rising interface forces. A plausible explanation is the relative motion of the leg pad along the thigh during flexion, which increases the effective moment arm

relative to the hip joint. This is supported by motion capture evidence of cumulative displacement. This cumulative displacement, possibly influenced by initial alignment offsets, is consistent with patterns observed by Akiyama et al. (2012), who employed a leg dummy to investigate the impact of joint misalignment on interface displacement during flexion. Such initial misalignment is difficult to eliminate in real-world applications, where precise alignment between the device and the anatomical hip joint is inherently challenging. The hip joint's complex multi-axis kinematics, involving both translation and rotation (Öhlin et al., 2025), further complicates alignment. Self-aligning mechanisms offer potential mitigation for motion-induced misalignment via passive degrees of freedom (Beil et al., 2017), but they introduce mechanical complexity. The observed hysteresis amplification likely results from a combination of pad slippage—inducing frictional energy loss—and joint coordination that enhances path-dependent differences between flexion and extension. These findings suggest that minimizing misalignment and aligning assistance with joint coordination dynamics may reduce energy loss and enhance the mechanical effectiveness of back-support exoskeletons.

Several limitations should be acknowledged in this study. First, the lack of programmable actuation limits systematic investigation of joint coordination effects on mechanical interactions. Second, the evaluation was limited to a simulated flexion–extension task. Broader task scenarios involving asymmetric lifting and trunk rotation are needed to generalize the findings. Third, the study included only three experimental trials, despite exhibiting high internal consistency, and remains insufficient to support statistically robust conclusions. Finally, while the sensorized manikin is designed to accommodate various back-support exoskeletons, this study evaluated only one device. As a result, the generalizability of the findings to other exoskeletons remains to be established.

In summary, this study introduced a sensorized multi-joint manikin capable of quantifying mechanical interactions between back-support exoskeletons and the body during bending-like motion. The platform enables simultaneous measurement of segmental normal and tangential forces and assistive torque, and permits observational analysis of how joint coordination influences these mechanical variables. These capabilities may support biomechanical modeling, inform exoskeleton design, and facilitate comparisons across devices. Future work may incorporate motorized actuation to control joint kinematics and extend testing to additional exoskeletons and movement scenarios.

## Acknowledgements

Conceptualization, H.T., T.T.; methodology, H.T., T.T.; setup design, H.T., T.T., H.C.; draft preparation, H.T.; writing—review and editing, H.T., T.T., H.C., J.G., T.V., B.V.; All authors have read and agreed to the published version of the manuscript.

During the preparation of this work, the authors used ChatGPT by OpenAI in order to improve phrasing and language clarity. After using this tool, the authors reviewed and edited the content as needed and take full responsibility for the content of the publication.

This project was funded by the CSC Scholarship.

## References

- Akiyama, Y., Okamoto, S., Yamada, Y., Ishiguro, K., 2015. Measurement of contact behavior including slippage of cuff when using wearable physical assistant robot. *IEEE Transactions on Neural Systems and Rehabilitation Engineering* 24, 784–793.
- Akiyama, Y., Yamada, Y., Ito, K., Oda, S., Okamoto, S., Hara, S., 2012. Test method for contact safety assessment of a wearable robot—analysis of load caused by a misalignment of the knee joint, in: 2012 IEEE RO-MAN: the 21st IEEE international symposium on robot and human interactive communication, IEEE. pp. 539–544.
- Armitage, L., Turner, S., Sreenivasa, M., 2021. Human-device interface pressure measurement in prosthetic, orthotic and exoskeleton applications: A systematic review. *Medical Engineering & Physics* 97, 56–69.
- Beil, J., Marquardt, C., Asfour, T., 2017. Self-aligning exoskeleton hip joint: Kinematic design with five revolute, three prismatic and one ball joint, in: 2017 International Conference on Rehabilitation Robotics (ICORR), IEEE. pp. 1349–1355.
- Bessler, J., Prange-Lasonder, G.B., Schaake, L., Saenz, J.F., Bidard, C., Fassi, I., Valori, M., Lassen, A.B., Buurke, J.H., 2021. Safety assessment of rehabilitation robots: A review identifying safety skills and current knowledge gaps. *Frontiers in Robotics and AI* 8, 602878.
- Brouwer, N.P., Tabasi, A., Hu, F., Kingma, I., van Dijk, W., Refai, M.I.M., van der Kooij, H., van Dieën, J.H., 2024. The effect of active exoskeleton support with different lumbar-to-hip support ratios on spinal musculoskeletal loading and lumbar kinematics during lifting. *Wearable Technologies* 5, e25.
- Choi, H., Seo, K., Hyung, S., Shim, Y., Lim, S.C., 2018. Compact hip-force sensor for a gait-assistance exoskeleton system. *Sensors* 18, 566.
- Dežman, M., Massardi, S., Pinto-Fernandez, D., Grosu, V., Rodriguez-Guerrero, C., Babič, J., Torricelli, D., 2023. A mechatronic leg replica to benchmark human–exoskeleton physical interactions. *Bioinspiration & Biomimetics* 18, 036009.

- Eskandari, A.H., Ghezelbash, F., Shirazi-Adl, A., Arjmand, N., Larivière, C., 2025. Effect of a back-support exoskeleton on internal forces and lumbar spine stability during low load lifting task. *Applied Ergonomics* 123, 104407.
- Hilmi, A.H., Hamid, A.R.A., Ibrahim, W.A.R.A.W., 2024. Current trends and risk factors in low back pain: An ergonomic perspective on prevention and management. *Malaysian Journal of Ergonomics (MJEr)* 6, 105–118.
- Koopman, A.S., Kingma, I., Faber, G.S., de Looze, M.P., van Dieën, J.H., 2019. Effects of a passive exoskeleton on the mechanical loading of the low back in static holding tasks. *Journal of biomechanics* 83, 97–103.
- Koopman, A.S., Kingma, I., de Looze, M.P., van Dieën, J.H., 2020a. Effects of a passive back exoskeleton on the mechanical loading of the low-back during symmetric lifting. *Journal of biomechanics* 102, 109486.
- Koopman, A.S., Näf, M., Baltrusch, S.J., Kingma, I., Rodriguez-Guerrero, C., Babič, J., de Looze, M.P., van Dieën, J.H., 2020b. Biomechanical evaluation of a new passive back support exoskeleton. *Journal of Biomechanics* 105, 109795.
- Langlois, K., Rodriguez-Cianca, D., Serrien, B., De Winter, J., Verstraten, T., Rodriguez-Guerrero, C., Vanderborght, B., Lefeber, D., 2020. Investigating the effects of strapping pressure on human-robot interface dynamics using a soft robotic cuff. *IEEE transactions on Medical Robotics and Bionics* 3, 146–155.
- Luckhaupt, S.E., Dahlhamer, J.M., Gonzales, G.T., Lu, M.L., Groenewold, M., Sweeney, M.H., Ward, B.W., 2019. Prevalence, recognition of work-relatedness, and effect on work of low back pain among us workers. *Annals of Internal Medicine* 171, 301–304.
- Madinei, S., Kim, S., Park, J.H., Srinivasan, D., Nussbaum, M.A., 2022. A novel approach to quantify the assistive torque profiles generated by passive back-support exoskeletons. *Journal of Biomechanics* 145, 111363.
- Massardi, S., Rodríguez-Cianca, D., Pinto-Fernandez, D., Moreno, J.C., Lancini, M., Torricelli, D., 2022. Characterization and evaluation of human–exoskeleton interaction dynamics: a review. *Sensors* 22, 3993.
- Olafsson, G., Jonsson, E., Fritzell, P., Hägg, O., Borgström, F., 2018. Cost of low back pain: results from a national register study in sweden. *European Spine Journal* 27, 2875–2881.
- Pal, P., Milosavljevic, S., Sole, G., Johnson, G., 2007. Hip and lumbar continuous motion characteristics during flexion and return in young healthy males. *European Spine Journal* 16, 741–747.
- van Sluijs, R.M., Wehrli, M., Brunner, A., Lamercy, O., 2023. Evaluation of the physiological benefits of a passive back-support exoskeleton during lifting and working in forward leaning postures. *Journal of Biomechanics* 149, 111489.
- Theurel, J., Desbrosses, K., 2019. Occupational exoskeletons: overview of their benefits and limitations in preventing work-related musculoskeletal disorders. *IIEE Transactions on Occupational Ergonomics and Human Factors* 7, 264–280.
- Thomas, J.S., Gibson, G.E., 2007. Coordination and timing of spine and hip joints during full body reaching tasks. *Human movement science* 26, 124–140.
- Tsang, S.M., Szeto, G.P., Li, L.M., Wong, D.C., Yip, M.M., Lee, R.Y., 2017. The effects of bending speed on the lumbo-pelvic kinematics and movement pattern during forward bending in people with and without low back pain. *BMC musculoskeletal disorders* 18, 1–11.
- Van Harmelen, V., Schnieders, J., Wagemaker, S., 2022. Measuring the amount of support of lower back exoskeletons. *Laevo White Paper*.
- Vazirian, M., Van Dillen, L.R., Bazrgari, B., 2016. Lumbopelvic rhythm in the sagittal plane: A review of the effects of participants and task characteristics. *International musculoskeletal medicine* 38, 51–58.
- Wang, S., Zhang, B., Yu, Z., Yan, Y., 2021. Differential soft sensor-based measurement of interactive force and assistive torque for a robotic hip exoskeleton. *Sensors* 21, 6545.
- Wei, W., Wang, W., Qu, Z., Gu, J., Lin, X., Yue, C., 2020. The effects of a passive exoskeleton on muscle activity and metabolic cost of energy. *Advanced Robotics* 34, 19–27.
- Wenig, C.M., Schmidt, C.O., Kohlmann, T., Schweikert, B., 2009. Costs of back pain in germany. *European journal of pain* 13, 280–286.
- Weston, E.B., Alizadeh, M., Knapik, G.G., Wang, X., Marras, W.S., 2018. Biomechanical evaluation of exoskeleton use on loading of the lumbar spine. *Applied ergonomics* 68, 101–108.
- Öhlin, A., Lindman, I., Karlsson, L., Sansone, M., 2025. *Hip Anatomy and Biomechanics*. Springer Nature Switzerland, Cham. pp. 1573–1580.